

Ageostrophic Secondary Circulation in a Subtropical Intrathermocline Eddy

BÀRBARA BARCELÓ-LLULL

Instituto de Oceanografía y Cambio Global, Universidad de Las Palmas de Gran Canaria, Telde, Spain

ENRIC PALLÀS-SANZ

Centro de Investigación Científica y Educación Superior de Ensenada, Ensenada, México

PABLO SANGRÀ AND ANTONIO MARTÍNEZ-MARRERO

Instituto de Oceanografía y Cambio Global, Universidad de Las Palmas de Gran Canaria, Telde, Spain

SHEILA N. ESTRADA-ALLIS

Centro de Investigación Científica y Educación Superior de Ensenada, Ensenada, México

JAVIER ARÍSTEGUI

Instituto de Oceanografía y Cambio Global, Universidad de Las Palmas de Gran Canaria, Telde, Spain

(Manuscript received 16 November 2016, in final form 7 March 2017)

ABSTRACT

Vertical motions play a key role in the enhancement of primary production within mesoscale eddies through the introduction of nutrients into the euphotic layer. However, the details of the vertical velocity field w driving these enhancements remain under discussion. For the first time the mesoscale w associated with an intrathermocline eddy is computed and analyzed using in situ high-resolution three-dimensional (3D) fields of density and horizontal velocity by resolving a generalized omega equation valid for high Rossby numbers. In the seasonal pycnocline the diagnosed w reveals a multipolar structure with upwelling and downwelling cells located at the eddy periphery. In the main pycnocline w is characterized by a dipolar structure with downwelling velocities upstream of the propagation path and upwelling velocities downstream. Maximum values of w reach 6.4 m day^{-1} . An observed enhancement of chlorophyll-*a* at the eddy periphery coincides with the location of the upwelling and downwelling cells. Analysis of the forcing terms of the generalized omega equation indicates that the mechanisms behind the dipolar structure of the w field are a combination of horizontal deformation and advection of vertical relative vorticity by ageostrophic vertical shear. The wind during the eddy sampling was rather constant and uniform with a speed of 5 m s^{-1} . Diagnosed nonlinear Ekman pumping leads to a dipolar pattern that mirrors the inferred w . Horizontal ageostrophic secondary circulation is dominated by centripetal acceleration and closes the dipole w structure. Vertical fluxes act to maintain the intrathermocline eddy structure.

1. Introduction

Mesoscale eddies are ubiquitous features of the World Ocean and are associated with important biogeochemical activity due to both their horizontal and vertical motions (McGillicuddy 2016). There are two types of eddies depending on their sense of rotation: anticyclonic

eddies, which have negative (positive) vertical relative vorticity, and cyclonic eddies, which are characterized by positive (negative) vertical relative vorticity in the Northern (Southern) Hemisphere. A particular type of anticyclones is intrathermocline eddies, which are subsurface intensified eddies also rotating anticyclonically but with dome-shaped (bowl shaped) isopycnals in the upper (lower) layers (McGillicuddy et al. 2007).

Ageostrophic secondary circulation (ASC), which includes the ageostrophic horizontal velocity and the

Corresponding author: Bàrbara Barceló-Llull, b.barcelo.llull@gmail.com

vertical velocity, has an important role within mesoscale structures through the restoring of thermal wind balance. The vertical velocities associated with ASC play an important role in the oceanic vertical pump (Klein and Lapeyre 2009), which has been defined as those physical processes, mainly at the submesoscale range [spatial scales below the first baroclinic Rossby deformation radius, 0.1–10 km (Shcherbina et al. 2015)], that drive intense nutrient fluxes into the euphotic layer, changing the plankton community structure and enhancing primary production and, hence, having a major impact on the marine carbon cycle. Measuring vertical velocities in the ocean is challenging because of their small order of magnitude when compared with horizontal velocities, $W \sim (10^{-3}\text{--}10^{-4})U \sim 10\text{ m day}^{-1}$ for the mesoscale and $W \sim (10^{-2})U \sim 100\text{ m day}^{-1}$ for the submesoscale (Mahadevan and Tandon 2006). Attempts to measure vertical velocities in the ocean include tracer release experiments and Lagrangian isopycnal drifter measurements (Hansen and Paul 1987; Schultz Tokos et al. 1994; Lindstrom and Watts 1994; McGillicuddy et al. 2007; Harcourt et al. 2002; D'Asaro et al. 2011). Although these attempts have provided an estimate of vertical velocities, they have not been able to give details of the corresponding fields and, thus, details of the forcing mechanisms. As detailed next, with this purpose different approaches were envisaged through the inference of the vertical velocity field from the sampled density and horizontal velocity fields using distinct forms of the so-called omega equation or inverse methods (Viúdez et al. 1996; Thomas et al. 2010).

Methods to infer vertical velocity from diagnostic equations in geophysical flows were first derived for the atmosphere. Hoskins et al. (1978) used quasigeostrophic theory (QG) to diagnose vertical motion in the atmosphere by implementing the Q vector form of the omega equation that is valid for the low Rossby number (Ro) regime. In their formulation, QG vertical velocity results from the adjustment process that takes place when thermal wind balance is destroyed by the geostrophic deformation field (Durrán and Snellman 1987). Tintoré et al. (1991) and Pollard and Regier (1992) reformulated the QG omega equation for the ocean in order to estimate vertical velocities in oceanic mesoscale frontal regions. Since these earlier studies, the QG omega equation has been widely applied to infer vertical velocities in oceanic mesoscale features, taking advantage of the fact that only the measured density field and related variables are needed (Shearman et al. 2000; Martin and Richards 2001; Rodríguez et al. 2001; Benítez-Barrios et al. 2011; Pascual et al. 2015; Barceló-Llull et al. 2016). Further developments of the omega equation in order to provide more accuracy in the diagnosis

of vertical velocity include the ageostrophic advection of geostrophic velocity leading to the so-called semigeostrophic (SG) omega equation (Hoskins and Draghici 1977). This ageostrophic advection becomes relevant where there are significant horizontal variations in static stability and potential vorticity, such as in sharp fronts, leading to high Ro and thus invalidating the QG form (Pedder and Thorpe 1999; Badin 2012). As for the QG form, the SG form allows, in practice, the computation of vertical velocity from geostrophic flow as obtained from density measurements only (Pinot et al. 1996).

Prior to the reformulation by Hoskins et al. (1978) into the Q vector form, the first formulation of the omega equation presented an undesirable cancellation of the forcing terms that made determination of their relative strengths extremely difficult (Trenberth 1978). To solve this difficulty, Viúdez et al. (1996) proposed a generalized form of the omega equation for the ocean in terms of the material rate of change of the differential ageostrophic vertical relative vorticity, instead of the local rate of change of the differential geostrophic vertical relative vorticity. Using primitive equation numerical experiments, Viúdez and Dritschel (2004) tested the accuracy of the three cited forms of the omega equation, concluding that the generalized form was the most accurate in the diagnosis of vertical velocities. Therefore, the generalized omega equation of Viúdez et al. (1996) is both less restrictive and more accurate than the Q vector-based QG and SG forms and, in addition, it allows vertical velocity diagnoses in highly ageostrophic environments. However, as it is primitive equation based, one disadvantage of this form is that it requires measurements of both the density and horizontal velocity fields. As in this study we have accurately measured both these fields, we will apply the generalized omega equation form derived by Viúdez et al. (1996) for the diagnosis of vertical velocities in our sampled subtropical intrathermocline eddy.

As the alongfront flow may be considered linear, vertical velocity in mesoscale frontal regions can only be diagnosed from cross-front vertical sections of density (QG and SG omega equation forms) or from both cross-front vertical sections of density and horizontal velocity (generalized omega equation form). Two-dimensional and three-dimensional diagnoses have contributed to a better understanding of ASCs and the associated processes in these regions (Pollard and Regier 1992; Allen and Smeed 1996; Naveira Garabato et al. 2001; Pallàs-Sanz et al. 2010a,b). However, in the case of mesoscale eddies, as the flow is nonlinear, a three-dimensional (3D) quasi-synoptic grid of the above fields is needed to diagnose vertical

velocity with a generalized omega equation. For this reason, studies of ASCs in mesoscale eddies are notably more scarce than they are in frontal regions. [Allen and Smeed \(1996\)](#) diagnose the vertical velocity at the Iceland–Færøes Front and the related eddy field using the QG omega equation from density data obtained from SeaSoar tracks. Their Fig. 11 shows a dipolar structure for the vertical velocity related with a cyclonic eddy, with an upwelling cell on one side and a downwelling cell on the other. However, because of the low resolution between SeaSoar tracks (50 km), it is difficult to well establish the details of such variability. They relate this dipolar pattern to vortex stretching. [Martin and Richards \(2001\)](#) also diagnose the vertical velocity field in an intrathermocline eddy using the QG omega equation, obtaining a multipolar vertical velocity distribution that may be consistent with an azimuthal perturbation of the eddy shape. However, the inferred vertical velocity field shows significant errors that arise from the necessary compromise between the spatial resolution and the synopticity of the eddy sampling ([Klein and Lapeyre 2009](#)). [Benítez-Barríos et al. \(2011\)](#) estimate the QG vertical velocity in an intrathermocline eddy in the northwest (NW) African coastal transition zone. Their low-resolution data also suggest a dipolar structure for the QG vertical velocity field with a downwelling (upwelling) cell in the western (eastern) side. [Buongiorno Nardelli et al. \(2001\)](#) infer the QG vertical velocity in a cyclonic eddy in the Atlantic–Ionian stream, finding also a dipolar distribution of QG vertical velocity. More recently, [Buongiorno Nardelli \(2013\)](#) estimated the vertical velocity in a cyclonic Aghulas ring using the SG omega equation from combined satellite–in situ synthetic reconstructed data. His results show that the vertical velocity field is organized in a dipolar pattern within the eddy core and in an octopolar pattern along the eddy periphery consisting of alternating upwelling and downwelling cells. He suggests that these patterns could be related with vortex Rossby waves ([McWilliams et al. 2003](#)). [Barceló-Llull et al. \(2016\)](#) also diagnose the QG vertical velocity field in the southeast Pacific from a similar synthetic observation-based product combining satellite and in situ data. With this low-resolution data ($1/3^\circ$) they find dipolar distributions of vertical velocity within mesoscale eddies.

Related with the difficulty of obtaining 3D quasi-synoptic fields with enough resolution, most of the studies of ASC in mesoscale eddies have been oriented toward the particular process of the self-induced Ekman pumping, paying particular attention to its effects on chlorophyll-*a* distribution ([Gaubé et al. 2014, 2015](#)). Three mechanisms have been identified that

are linked with this process ([Gaubé et al. 2015](#)). The first mechanism results from the wind stress curl induced by the differences between surface winds and ocean velocities that give rise to an Ekman upwelling (downwelling) at the cores of anticyclones (cyclones) ([Martin and Richards 2001](#); [McGillicuddy et al. 2007](#); [Gaubé et al. 2015](#)). As formulated by [Stern \(1965\)](#), the second mechanism arises from the interaction of the surface wind stress with the surface geostrophic vertical vorticity gradient and results in mesoscale dipoles of Ekman upwelling and downwelling ([McGillicuddy et al. 2008](#); [Gaubé et al. 2015](#)). When the eddy periphery contains a submesoscale frontal region, it has been proposed that this second mechanism also leads to Ekman dipoles but only at the periphery and at the submesoscale range ([Mahadevan et al. 2008](#)). The third mechanism is secondary, and it is associated with the wind stress curl induced by sea surface temperature gradients ([Chelton and Xie 2010](#); [Gaubé et al. 2015](#)). The first mechanism is named linear Ekman pumping, and the second is named nonlinear Ekman pumping ([McGillicuddy et al. 2008](#); [Gaubé et al. 2015](#)).

There is growing evidence to indicate that anticyclonic eddies may be as productive as cyclonic ones in the enhancement of primary production [see recent review of [McGillicuddy \(2016\)](#)]. However, the details and mechanisms responsible for such enhancement are still under discussion. [McGillicuddy et al. \(2007\)](#) observed an extraordinary phytoplankton bloom at the core of a subtropical intrathermocline eddy and proposed that linear Ekman pumping was the mechanism responsible. Alternatively, [Mahadevan et al. \(2008\)](#), using numerical modeling, proposed that phytoplankton enhancement occurs at the eddy periphery at the submesoscale range due to the nonlinear Ekman mechanism and is then advected toward its core. Composite averages of chlorophyll-*a* and linear Ekman pumping as obtained from satellite data support the enhancement of chlorophyll-*a* at anticyclonic eddy cores due to linear Ekman pumping ([Gaubé et al. 2013, 2014](#)). However, as shown in Fig. 3 of [Calil and Richards \(2010\)](#), instantaneous fields of altimetry and chlorophyll-*a* indicate that this enhancement occurs at the eddy periphery instead of at the eddy core, nonlinear Ekman pumping being a plausible candidate for such enhancement.

As already mentioned, there are few studies of ASC in mesoscale eddies due to the difficulty in obtaining quasi-synoptic 3D fields with high resolution. On the other hand, most of the attempts to investigate the influence of mesoscale eddies on chlorophyll-*a* distributions are based on remote sensing observations, due also to the

difficulty in obtaining 3D in situ fields. Furthermore, these studies focus only on the self-induced Ekman pumping process without diagnosing the vertical velocity field as a result of all processes causing vertical motions as formulated by the generalized omega equation. To fill this gap, in September 2014 we conducted an interdisciplinary survey of a subtropical intrathermocline eddy in the framework of the Study of the Vertical Oceanic Pump in mesoscale eddies (PUMP) project. A detailed description of the eddy structure and dynamics may be found in [B. Barceló-Llull et al. \(2017\)](#). Here we describe and discuss the eddy ASC and its role in chlorophyll-a enhancement using high-resolution quasi-synoptic 3D in situ fields.

2. Data and methods

a. Dataset and optimal interpolation

The PUMP interdisciplinary survey of a subtropical intrathermocline eddy was carried out from 3 to 20 September 2014 aboard the R/V *BIO Hespérides*. The PUMP eddy was generated 4 months earlier at the island of Tenerife in the Canary Islands. The Canary Islands continuously spin off mesoscale eddies that form the so-called Canary Eddy Corridor, which is the main pathway for long-lived eddies in the subtropical northeast Atlantic ([Sangrà et al. 2009](#)). Guided by its signal in altimetric sea level anomaly (SLA) fields, we first crossed the eddy with two transects sampled with continuous tows of a conductivity–temperature–depth (CTD) probe on an undulating vehicle (SeaSoar MK II) during the days 3–5 September 2014 ([Fig. 1](#), black dashed lines) to locate the eddy center and determine its size. Then, in order to obtain the 3D fields for the diagnosis of vertical velocities, we sampled a grid centered on the eddy center. The grid consisted of six SeaSoar ([Fig. 1](#), gray lines) and three discrete CTD (the SeaSoar CTD was attached to a CTD rosette system after a failure of the SeaSoar; [Fig. 1](#), gray dots) zonal transects of length 90 nautical miles (nmi; 1 nmi = 1.852 km); the distance between the transects was 10 nmi. The rosette stations were also 10 nmi apart, while the SeaSoar undulating vehicle provided profiles separated by 4 km with an effective vertical resolution of 72 cm. The rosette transects were completed in ~16 h, while the long (short) SeaSoar transects were completed in ~12 h (9 h) with a ship speed of 8 kt (1 kt = 0.51 m s^{-1}). The time of navigation between transects was ~1.5 h. The 3D survey was accomplished in 5 days (6–11 September 2014). With this sampling strategy we tried to reach a compromise between the spatial resolution and the synopticity of the eddy sampling

([Martin and Richards 2001](#)). [Allen et al. \(2001\)](#) study the implications on vertical velocity estimations of the errors associated with the sampling strategy. They analyze a sampling strategy similar to the PUMP survey to sample mesoscale structures consisting of transects separated by ~23 km and with an along-track resolution of ~5 km, considering a ship speed of ~8 kt, and with a total sampling duration of ~4.5 days. They find that the vertical velocity distribution remains unaltered, while its magnitude is reduced because of the smoothing introduced by the sampling resolution, without alterations due to the lack of synopticity. Hence, we may conclude that the PUMP survey followed a sampling strategy well compromised to estimate vertical motions.

The SeaSoar MK II measurements extended from 10 m down to 325 m, while discrete CTD casts were made to a nominal depth of 400 m. Both the SeaSoar MK II and CTD rosette systems were equipped with CTD SB911+ probes, additionally equipped with a Seapoint chlorophyll fluorometer sensor, which provided fluorescence measurements. Raw data files were processed with Sea-Bird Seasoft software (<http://www.seabird.com/software/softrev.htm>) and vertically averaged into 8-m bins. The International Thermodynamic Equation Of Seawater—2010 (TEOS-10) algorithms to calculate Absolute Salinity S_A and Conservative Temperature Θ and all derived variables were used ([Feistel 2003, 2008](#)). Chlorophyll-a concentrations were estimated from the in situ fluorescence provided by the fluorometer sensor previously calibrated with 256 samples of extracted chlorophyll-a, according to [Holm-Hansen et al. \(1965\)](#). The relationship between the readings of the fluorometer F and the chlorophyll-a concentration extracted from seawater samples (CHL) is $\text{CHL} (\text{mg m}^{-3}) = 0.5078F - 0.005$; $R^2 = 0.5773$; this was used to transform in situ fluorescence to actual chlorophyll-a.

In addition, current velocities were observed continuously through a hull-mounted RDI acoustic Doppler current profiler (ADCP) Ocean Surveyor, working at 75 kHz. The ADCP gave raw data with 5-min ensembles from the surface to 800-m depth and a bin size of 8 m. The raw data were quality controlled with the Common Oceanographic Data Access System (CODAS; [Firing et al. 1995](#)). On average, the controlled profiles provide good data from 21- to 625-m depth. The velocities were calibrated for transducer misalignment, adjusted from ship relative currents to absolute currents using GPS position measurements and spatially averaged each 0.09° .

The density and horizontal velocity data were objectively interpolated onto a regular grid ([Fig. 1](#), crosses)

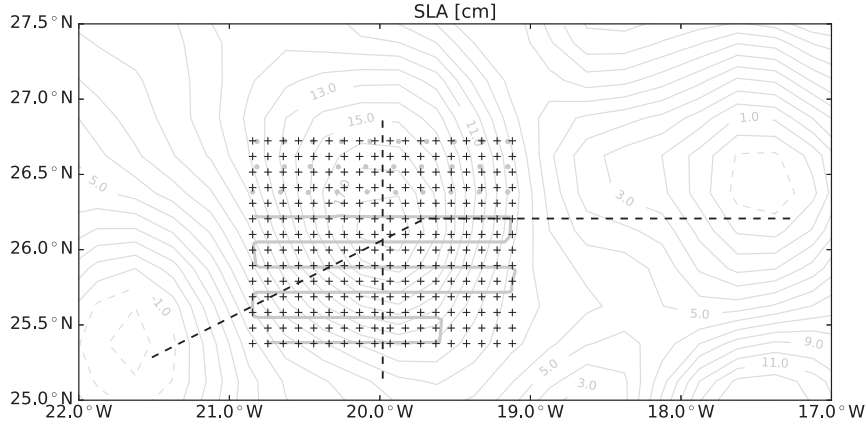


FIG. 1. Map of the PUMP eddy SLA (cm) signal from AVISO on 6 Sep 2014 (gray thin contours). Black dashed lines represent the SeaSoar transects to detect the eddy center. Thick gray lines and dots show the grid for the 3D eddy sampling with SeaSoar continuous tows and CTD casts, respectively. Black crosses represent the interpolation grid.

with a horizontal resolution of $0.1^\circ \times 0.1^\circ$ (\sim half the original resolution of 10 n mi) and a vertical resolution of 8 m (Bretherton et al. 1976). The data covariance was fitted with a 2D Gaussian function with semimajor and semiminor axes of $L_x = L_y = 40$ km. These correlation scales (L_x and L_y) were selected by analyzing the autocorrelation matrix of the observed fields and are of the order of the eddy radius. With this interpolation, wavelengths smaller than the correlation lengths of the covariance function are filtered (Le Traon 1990). This smoothing is important for solving the omega equation as it requires computing second-order spatial derivatives of the interpolated fields (Pallàs-Sanz et al. 2010a). The mean fields were assumed to be planar for density and constant for horizontal velocity (Rudnick 1996). The uncorrelated noise is set to 3% of the signal energy (Rudnick 1996; Pallàs-Sanz et al. 2010a). From chlorophyll-a data we estimated the deep chlorophyll-a maximum (DCM), which was objectively interpolated onto a horizontal grid of $0.1^\circ \times 0.1^\circ$ with the above Gaussian function and considering planar mean field.

b. Inference of the geostrophic flow and the generalized omega equation

The geostrophic flow is estimated from the observed density field through thermal wind balance, imposing the ADCP velocity at the deeper depth of the density dataset (325 m). Then, we estimate the ageostrophic horizontal velocity as the difference between the total (ADCP) horizontal velocity and the geostrophic velocity $\mathbf{u}_h^a = \mathbf{u}_h - \mathbf{u}^g$, where the superscript g denotes geostrophy, a denotes ageostrophy, and \mathbf{u}_h is the total horizontal velocity (Thomas et al. 2010).

The adiabatic generalized omega equation used in this study is the \mathbf{Q} vector form (Pallàs-Sanz and Viúdez 2005)

$$N^2 \nabla_h^2 w + f(f + \zeta) w_{zz} = \underbrace{2 \nabla_h \cdot \mathbf{Q}_h}_{S_{\text{DEF}}} + \underbrace{f \zeta_{ph}^a \cdot \nabla_h^2 \mathbf{u}_h}_{S_{\text{ADV}}}, \quad (1)$$

where $f = 2\Omega \sin\phi$ is the Coriolis parameter (considered constant and computed at the mean latitude ϕ), with Ω representing Earth's angular velocity ($f = 6.4 \times 10^{-5} \text{ s}^{-1}$); $N^2 = -g\alpha_0\rho_z$ is the Brunt-Väisälä frequency, where $\alpha_0 = \rho_0^{-1}$ is the mean specific volume, g is gravity, ρ is the density, and subscript z indicates a vertical derivative. Vertical relative vorticity is estimated as $\zeta = v_x - u_y$, where u and v are the zonal and meridional currents and x and y subscripts represent partial derivatives in the eastward and northward directions. The horizontal pseudovorticity vector is an anticlockwise rotation of the vertical shear, $\zeta_{ph} = (-v_z, u_z)$, while $\zeta_{ph}^a = (-v_z^a, u_z^a)$ is the ageostrophic horizontal pseudovorticity vector. The term ζ_{ph}^a can be viewed as the anticlockwise rotation of the thermal wind imbalance as $\mathbf{TWI} = (fu_z^a, fv_z^a)$, and hence $f\zeta_{ph}^a = \mathbf{k} \times \mathbf{TWI}$ (Giordani et al. 2006). The \mathbf{Q} vector represents the deformation of the horizontal density gradient by the total horizontal velocity field $\mathbf{Q} = \nabla_h \mathbf{u}_h \cdot \nabla_h b$, where $b = \rho g \alpha_0$ is the buoyancy.

The forcing terms of the generalized omega equation are on the right-hand side (rhs) of (1). The term S_{DEF} is related to the total deformation field and can be decomposed into its geostrophic and ageostrophic components: $S_{\text{DEF}} = S_{\text{DEFG}} + S_{\text{DEFA}}$. The term S_{ADV} is related to the vertical shear of the ageostrophic horizontal current through ζ_{ph}^a . Giordani et al. (2006) relate S_{ADV} with the stretching and reorientation of the

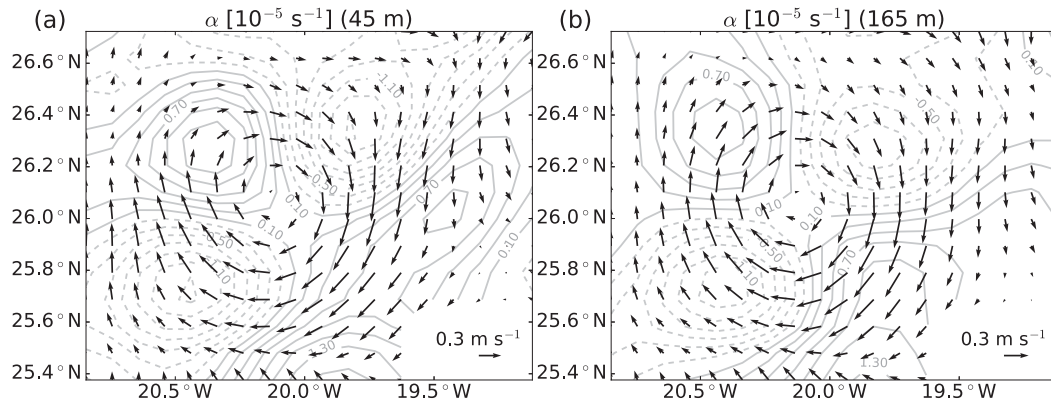


FIG. 2. Horizontal distribution of the deformation field α (10^{-5} s^{-1}) in gray contours at (a) 45- and (b) 165-m depth. Solid contours represent diffluent flow ($\alpha > 0$) and dashed contours confluent flow ($\alpha < 0$). Vectors indicate the ADCP velocity.

preexisting ζ_{ph}^a by the total horizontal current field. On the left-hand side (lhs) of (1) an elliptic operator (if $f + \zeta \geq 0$) is applied to the vertical velocity w . The resulting elliptic equation is solved with an iterative relaxation method and constrained by Dirichlet boundary conditions, that is, $w = 0$.

To analyze the accuracy of the derived geostrophic field including the ADCP velocity at the reference level (325-m depth), we alternatively estimated the geostrophic field by using the method proposed by Rudnick (1996) based on the imposition of constraints such as the horizontal nondivergence of the velocity field. The derived ageostrophic horizontal velocity obtained subtracting the constrained geostrophic velocity to the ADCP velocity showed the same vertical shear as the field estimated through the thermal wind balance, being the magnitude smaller. The slight difference in magnitude between the estimated fields with each methodology only affects the S_{DEFG} and S_{DEFA} forcing terms.

c. Wind-induced vertical velocities

Wind-induced vertical motions arise from the force of the surface wind stress $\boldsymbol{\tau} = (\tau^x, \tau^y, 0)$ (supercripts x and y denote eastward and northward components) through Ekman pumping. The wind speed field during the PUMP cruise is obtained from the Weather Research and Forecasting (WRF) Model (Skamarock et al. 2008). The surface wind stress, considering eddy–wind interaction, is estimated from the bulk formula:

$$\boldsymbol{\tau} = \rho_a C_D \mathbf{u}_{\text{rel}} |\mathbf{u}_{\text{rel}}|, \quad (2)$$

where $\rho_a = 1.3 \text{ kg m}^{-3}$ is the air density, and $C_D = 1.14 \times 10^{-3}$ is a drag coefficient considered constant with wind

velocities between 4 and 10 m s^{-1} (Large 1979). The relative wind speed is represented by $\mathbf{u}_{\text{rel}} = \mathbf{u}_a - \mathbf{u}_0$, where \mathbf{u}_a is the surface wind at 10 m above the mean sea level, and \mathbf{u}_0 is the surface ocean velocity. Ekman transport due to eddy–wind interaction can be written as (Stern 1965)

$$\mathbf{T}_E \simeq -\frac{\mathbf{k} \times \boldsymbol{\tau}}{\rho_0(f + \zeta_0)}, \quad (3)$$

and the associated Ekman pumping is

$$w_{\text{Ep}} = \nabla_h \cdot \mathbf{T}_E = \frac{\mathbf{k}}{\rho_0(f + \zeta_0)} \cdot \nabla_h \times \boldsymbol{\tau} + \frac{\mathbf{k} \times \boldsymbol{\tau}}{\rho_0(f + \zeta_0)^2} \cdot \nabla_h(f + \zeta_0), \quad (4)$$

where ρ_0 is the mean density (1026.4 kg m^{-3}), and ζ_0 is the geostrophic vertical relative vorticity at the sea surface. The first term on the rhs of (4) is the linear Ekman pumping, and it is related to the wind stress curl. The second term on the rhs of (4) is the nonlinear Ekman pumping, which is proportional to the advection of absolute vorticity by the Ekman transport.

3. Results

a. Intrathermocline eddy structure

The PUMP eddy is an anticyclonic intrathermocline eddy characterized by a biconvex shape of the isopycnals with a doming (depression) of the upper (deeper) layers corresponding to the seasonal (main) pycnocline. At the time of the survey, the PUMP eddy was 4 months old with a vertical extension of 500-m and 46-km radius. The eddy had a subsurface dynamical core embedded between the seasonal and main

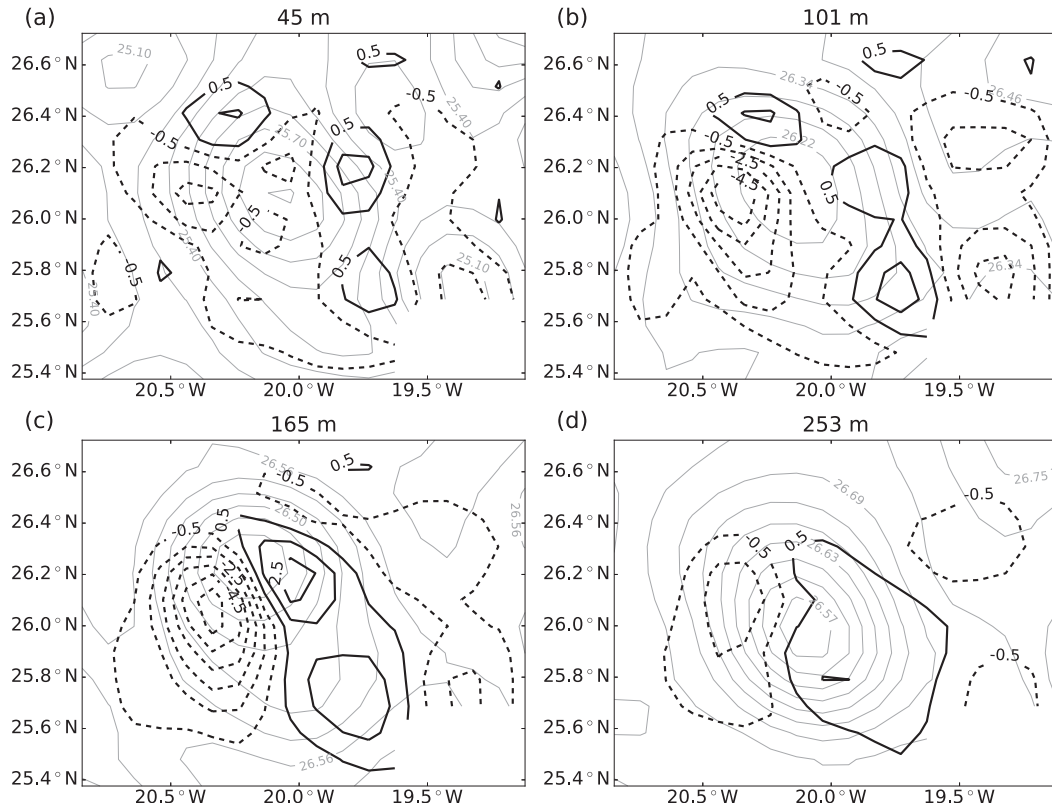


FIG. 3. Mesoscale vertical velocity w (m day^{-1}) in thick black contours (contour interval of 1 m day^{-1}) estimated from the generalized omega equation at different depths: (a) 45, (b) 101, (c) 165, and (d) 253 m. Thin gray contours represent the potential density anomaly σ_θ (kg m^{-3}) for reference.

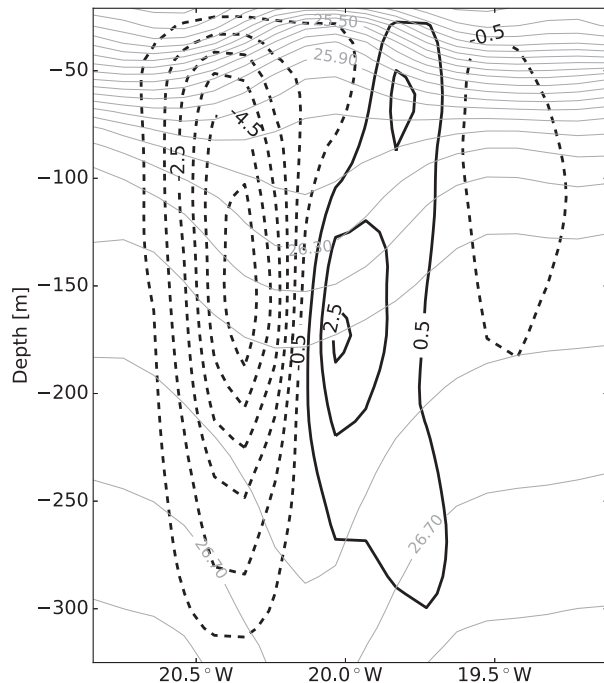
pycnoclines (centered at 85-m depth) with maximum horizontal velocities of 0.5 m s^{-1} . The subsurface horizontal velocity maximum is consistent with the typical biconvex intrathermocline eddy shape through thermal wind balance. Within the dynamical core the extreme Rossby number, $\text{Ro} = \zeta/f$, reaches -0.6 . Hence, the PUMP eddy is moderately ageostrophic, and the application of the QG approximation would neglect an important contribution of the ageostrophic horizontal motions, otherwise considered in the generalized omega equation used in this study. On the other hand, the eddy hydrographic core was located between 200- and 500-m depth and was characterized by warmer, saltier, and lighter anomalies of temperature, salinity, and density, respectively. A detailed description of the PUMP eddy is given by B. Barceló-Llull et al. (2017).

Figure 2 shows the horizontal distribution of the deformation field ($\alpha = u_x - v_y$) at 45 (domed seasonal pycnocline) and 165 m (depressed main pycnocline) with the ADCP velocity vectors superimposed. Alternating cells with confluent ($\alpha < 0$) and diffluent flows ($\alpha > 0$) are localized at the eddy periphery with maximum absolute values of $\sim 0.26f$. Confluent/diffluent

flow creates propitious conditions for thermal wind imbalance (TWI) and, in consequence, ASC (Hoskins and Bretherton 1972; Hoskins et al. 1978; Spall 1997). From the horizontal distribution of α , we expect ASC to arise at the eddy periphery.

b. Vertical velocity distribution and chlorophyll-*a* signature

Horizontal sections at different depths of the estimated vertical velocity within the PUMP eddy are shown in Fig. 3. In the upper layers, the vertical velocity distribution is characterized by small and weak upwelling ($w > 0$) and downwelling ($w < 0$) cells localized at the eddy periphery (Fig. 3a). Below 85-m depth, the horizontal distribution of w changes gradually to a dipolar pattern (Figs. 3b–d) with a downwelling (upwelling) cell on the western (eastern) edge of the anticyclonic eddy. At 165-m depth (Fig. 3c), the dipolar distribution of w reaches maxima of -6.3 and 3.3 m day^{-1} . Figure 4 shows a vertical section of the vertical velocity along 26.1°N . At this zonal section the dipolar distribution of w extends from the surface to the deepest available data depth



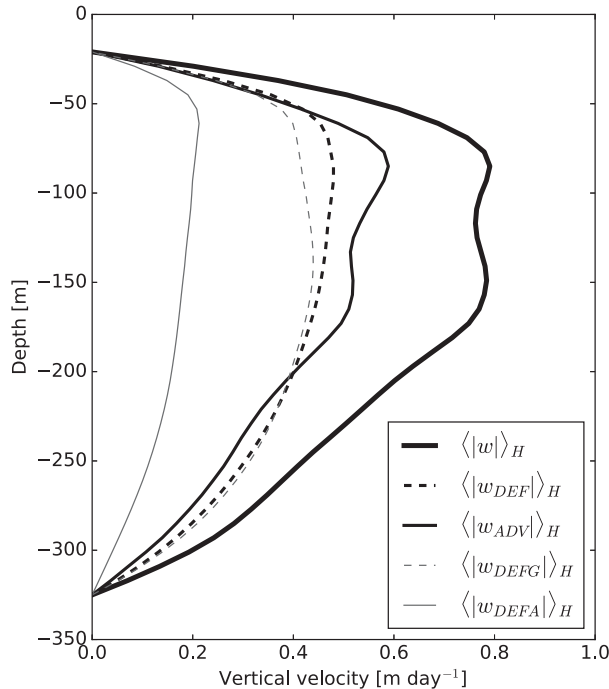


FIG. 6. Horizontal average of the absolute value of the vertical velocity estimated with each individual forcing term in (1), with the sum $S_{DEF} + S_{ADV}$, and with S_{DEFG} and S_{DEFA} .

w_{DEF} and w_{ADV} contributions give rise to the total vertical velocity distribution at 45-m depth (Fig. 3a). At 165-m depth (main pycnocline), w_{DEF} and w_{ADV} have slightly different orders of magnitude (Figs. 6, 8a,b). Maxima w_{DEF} of -2.2 and 2.5 m day^{-1} occur at the downwelling/upwelling cells located along the eddy periphery, while w_{ADV} extremum of -4.1 m day^{-1} is located at the western downwelling cell; the weaker eastern upwelling cell has maximum of 2.1 m day^{-1} . The w_{DEF} contribution is characterized by a quadripolar distribution, while w_{ADV} is characterized by an asymmetric dipolar pattern. Both vertical velocities contribute to the total vertical velocity distribution (Fig. 3c) characterized by a dipolar pattern with an intensified western downwelling cell and a broader eastern upwelling cell.

Although w_{DEF} and w_{ADV} have similar magnitudes over the whole water column and make similar contributions to the w distribution, w_{DEF} is mainly forced by its geostrophic component w_{DEFG} , as can be seen in Figs. 6, 7, and 8. The w_{DEFG} contribution estimated with the constrained geostrophic velocity obtained using the Rudnick (1996) method shows the same multipolar and quadripolar distributions with a negligible difference in shape and the same magnitude (not shown). Hence, the w distribution within the PUMP eddy is mainly driven by both w_{DEFG} and w_{ADV} .

d. Ekman pumping

Eddy-wind-induced Ekman pumping is derived following Stern (1965), and the wind stress is parameterized considering the eddy surface currents (section 2c). The wind stress computed from the bulk equation (2) has a spatially averaged value of $2.8 \times 10^{-2} \text{ N m}^{-2}$. Using this value, the Ekman layer depth is $\delta_E \simeq 0.4u^*/f = 32 \text{ m}$, where the frictional velocity is obtained from $u^* = \sqrt{|\tau|/\rho_0} = 5 \times 10^{-3} \text{ m s}^{-1}$ (Pallàs-Sanz et al. 2010a). Figure 9a shows the spatial distribution of the (scaled) geostrophic vertical relative vorticity at 21-m depth (ζ_0/f), which is the shallowest depth available, with the wind stress superimposed. The ζ_0 has minimum values at the eddy center of $-0.34f$ and a positive vorticity ($\zeta_0 > 0$) belt surrounding it. The direction of the wind stress is defined by the direction of the trade winds. The resulting Ekman transport is directed 90° clockwise to the wind stress direction.

The total Ekman pumping w_{Ep} and its linear and nonlinear components are shown in Fig. 9. The wind stress curl was small during the sampling of the PUMP eddy. As a consequence, the linear Ekman pumping in the PUMP eddy (Fig. 9c) has small values of 0.1 m day^{-1} at the eddy center, a magnitude smaller than the inferred vertical velocity using the omega equation. On the other hand, nonlinear Ekman pumping (Fig. 9d) has higher maximum values of 0.5 m day^{-1} and a dipolar distribution centered at the eddy core and oriented along the direction of the Ekman transport, that is, $w < 0$ ($w > 0$) at the western (eastern) edge of the eddy. The resulting (total) Ekman pumping (Fig. 9b) has a dipolar distribution driven by the nonlinear component and reaches values of -0.7 and 0.5 m day^{-1} at the eddy periphery.

Ekman model provides an estimate of the vertical velocity at the base of the Ekman layer driven by the interaction between wind and ocean surface currents. This interaction is a diabatic process driven by turbulent momentum fluxes. To compare the estimated Ekman pumping with the vertical velocity field derived by resolving (1), we have also integrated the diabatic version of the generalized omega equation proposed by Pallàs-Sanz et al. (2010b), in which an additional forcing term related with the parameterized transfer of momentum is included. The vertical eddy viscosity is parameterized with a mixed layer depth (MLD) profile (Nagai et al. 2006). The vertical velocity field inferred through the diabatic version of the generalized omega equation has the same distribution inside the eddy region as the adiabatically derived vertical velocity, while an enhancement of w is found outside the eddy periphery where the MLD is deeper (not shown). On the other hand, the wind

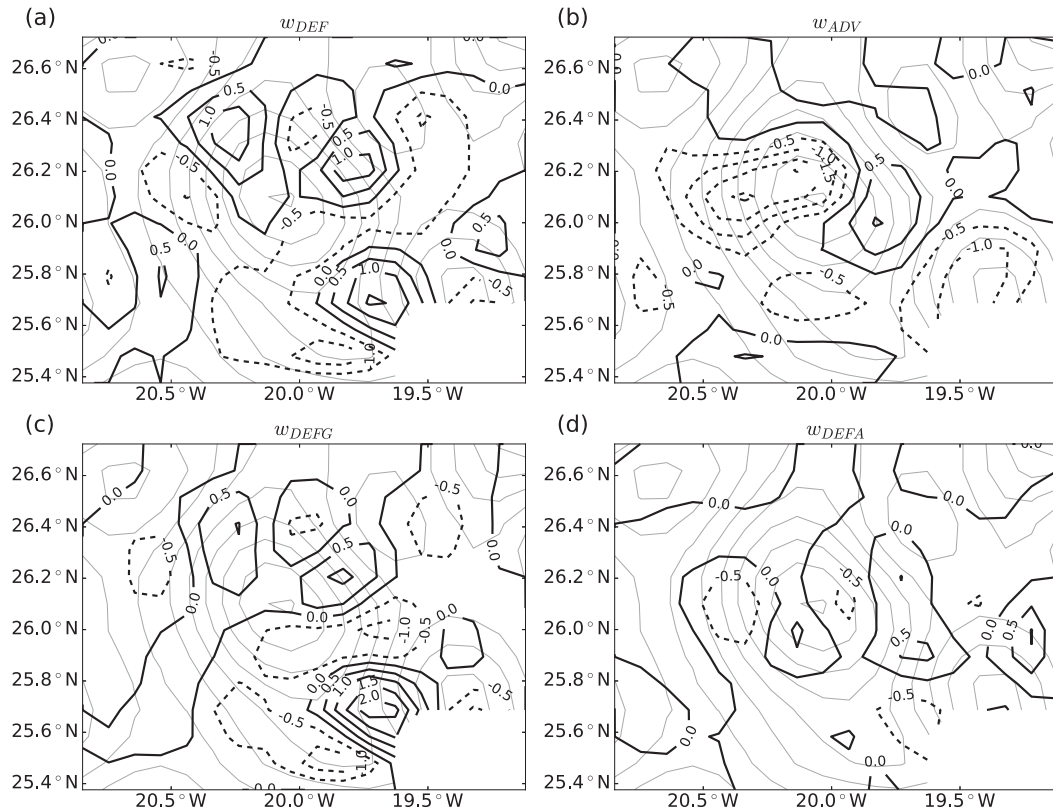


FIG. 7. Mesoscale vertical velocity w (m day^{-1}) in thick black contours (contour interval of 0.5 m day^{-1}) estimated with each individual forcing term in (1) at 45-m depth. Gray contours represent the potential density anomaly σ_θ for reference.

effects may also contribute significantly to the ageostrophic vertical shear used to construct S_{ADV} . Hence, a comparison of the Ekman pumping with the vertical velocity induced by the S_{ADV} forcing term is justified. Indeed, if we compare the total Ekman pumping distribution (Fig. 9b) with the w_{ADV} distribution at 45-m depth (Fig. 7b), we observe a similar dipolar pattern that is slightly rotated but with similar magnitude.

e. Horizontal ageostrophic secondary circulation

Figure 10a shows a vertical section along 26.1°N of the ASC zonal and vertical components (u^a , w). In the seasonal pycnocline, u^a is mainly directed westward and has maximum values of the order of 0.1 m s^{-1} located at the eddy periphery where the horizontal gradients of σ_θ are larger. In the deeper layers (between 175- and 265-m depth), u^a is directed to the east and advects flow from the downwelling cell to the upwelling cell to conserve mass in incompressible flow. Therefore, a cyclonic cell of ASC develops within the anticyclonic eddy.

The horizontal flow in the PUMP eddy is, on average, supergeostrophic as $|\mathbf{u}_h| > |\mathbf{u}^g|$ (B. Barceló-Llull et al. 2017).

Figure 10b shows the horizontal distribution of the horizontal ASC \mathbf{u}_h^a at 165-m depth, which is characterized by an anticyclonic circulation reaching maximum values of $\sim 0.07 \text{ m s}^{-1}$ at the eddy periphery. Horizontal ASC can be written using the inviscid horizontal momentum equation

$$\frac{D\mathbf{u}_h}{Dt} + f\mathbf{k} \times \mathbf{u}_h^a = 0 \quad (5)$$

as (e.g., Pallàs-Sanz and Viúdez 2007)

$$\mathbf{u}_h^a = \frac{1}{f}\mathbf{k} \times \frac{D\mathbf{u}_h}{Dt} = \frac{1}{f}\mathbf{k} \times \left(\frac{\partial \mathbf{u}_h}{\partial t} + \mathbf{u}_h \cdot \nabla_h \mathbf{u}_h + w \frac{\partial \mathbf{u}_h}{\partial z} \right). \quad (6)$$

Hence, in accordance with (6), the horizontal ASC can be interpreted as an anticlockwise rotation of the material rate of change of the (total) horizontal velocity. With the PUMP eddy dataset, that is, only one realization, we are not able to estimate the local temporal rate of change of the horizontal velocity. On the other hand, within the PUMP eddy the horizontal advective acceleration is two orders of magnitude higher than the vertical advective acceleration (not shown). Figure 10c

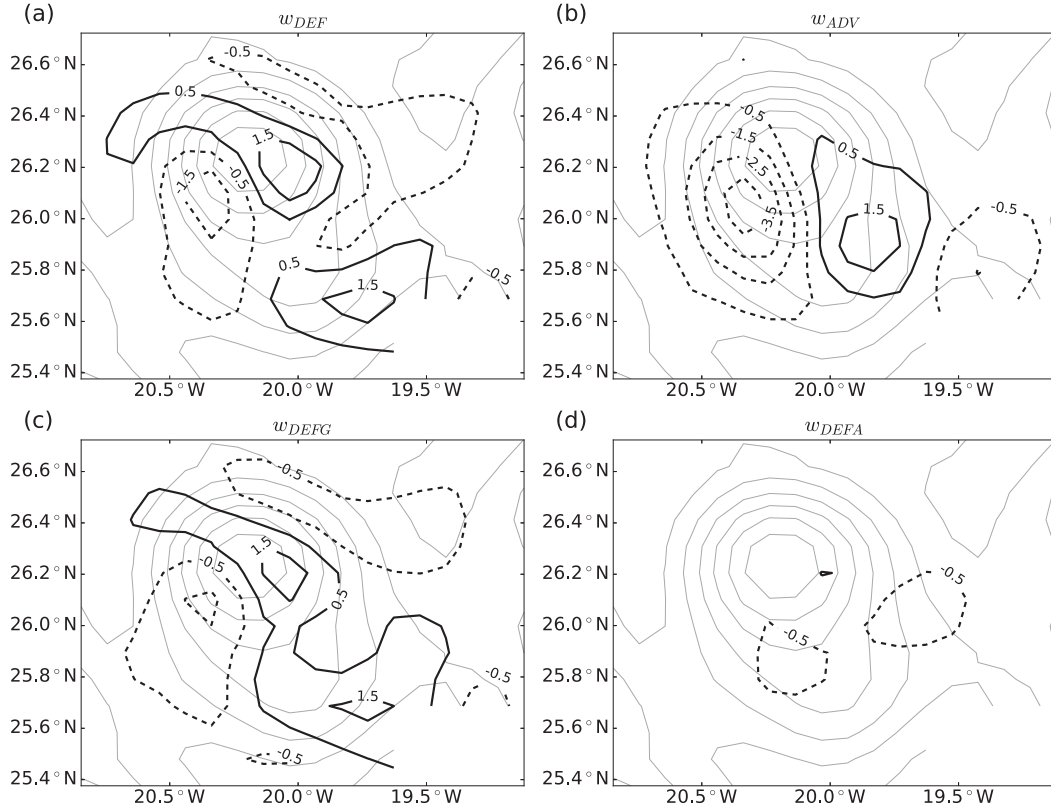


FIG. 8. As in Fig. 7, but for 165-m depth (contour interval of 1 m day^{-1}).

shows the horizontal distribution of this term scaled by the planetary vorticity f at 165-m depth. It points to the eddy center and has orders of magnitude of 0.05 m s^{-1} . Hence, its anticlockwise rotation agrees with the direction and magnitude of the horizontal ASC (Fig. 10b) within the eddy core. Therefore, the horizontal advective acceleration within the PUMP eddy, $\mathbf{u}_h \cdot \nabla_h \mathbf{u}_h$, is the most important contribution to the horizontal ASC.

The horizontal advective acceleration in the ($\mathbf{s} = \mathbf{u}_h / |\mathbf{u}_h|$, $\mathbf{n} = \mathbf{k} \times \mathbf{s}$) reference frame can be decomposed into two components:

$$\mathbf{u}_h \cdot \nabla_h \mathbf{u}_h = \frac{\delta}{\delta s} \left(\frac{u^2}{2} \right) \mathbf{s} + u^2 \kappa \mathbf{n}, \quad (7)$$

where κ is the streamline curvature, and $\delta/\delta s$ is the directional derivative along \mathbf{s} (Pallàs-Sanz and Viúdez 2007). The first term on the rhs of (7) is the speed acceleration, and the second term is the centripetal acceleration. As the horizontal advective acceleration clearly points to the eddy center (Fig. 10c), it is strongly suggested that the centripetal acceleration dominates the distribution. As a conclusion, horizontal ASC

within the PUMP eddy is mainly driven by the centripetal acceleration.

f. Interpretation of the sources of ASC

The forcing term S_{DEF} can be decomposed into two components:

$$S_{DEF} = 2\nabla_h \cdot \mathbf{Q}_h = 2\nabla_h \cdot (\nabla_h \mathbf{u}_h \cdot \nabla_h b) = 2\nabla_h^2 \mathbf{u}_h \cdot \nabla_h b + 2\nabla_h \mathbf{u}_h : \nabla_h (\nabla_h b),$$

and using the thermal wind balance relation $\nabla_h b = \mathbf{k} \times \mathbf{u}_z^g$ and the approximation $\nabla_h^2 \mathbf{u}_h \approx \mathbf{k} \times \nabla_h \zeta$ (Pallàs-Sanz and Viúdez 2005), S_{DEF} can be written as

$$S_{DEF} \approx 2f(\mathbf{k} \times \nabla_h \zeta) \cdot (\mathbf{k} \times \mathbf{u}_z^g) + 2\nabla_h \mathbf{u}_h : \nabla_h (\nabla_h b) = 2f \mathbf{u}_z^g : \nabla_h \zeta + 2\nabla_h \mathbf{u}_h : \nabla_h (\nabla_h b).$$

The first term is the horizontal advection of vertical relative vorticity by the geostrophic vertical shear, and the second term is related to a correlation between spatial changes of \mathbf{u}_h and $\nabla_h b$. A scale analysis of these two components shows similar orders of magnitude, and hence both terms contribute to the S_{DEF} forcing term. On the other hand, S_{ADV} can be

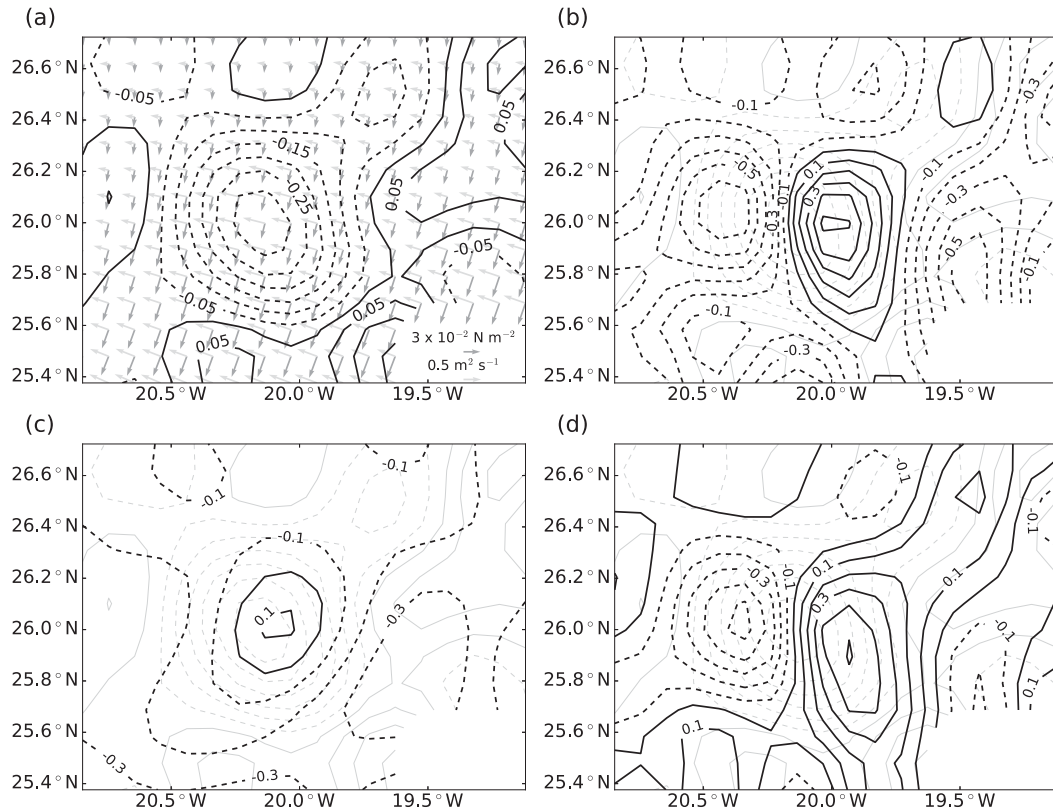


FIG. 9. (a) Scaled geostrophic relative vorticity at the sea surface (21 m) ζ_0/f in black contours. Wind stress assuming eddy-wind interaction τ is represented by dark gray arrows, while light gray arrows indicate Ekman transport \mathbf{T}_E . (b) Vertical motion (m day^{-1}) due to Ekman pumping w_{EP} and due to its (c) linear and (d) nonlinear components. In (b), (c), and (d) scaled geostrophic relative vorticity contours are plotted in light gray for reference.

approximated as the horizontal advection of vertical relative vorticity by the ageostrophic vertical shear:

$$S_{ADV} = f \zeta_{ph}^a \cdot \nabla_h^2 \mathbf{u}_h \approx f (\mathbf{k} \times \mathbf{u}_{hz}^a) \cdot (\mathbf{k} \times \nabla_h \zeta) \approx f \mathbf{u}_{hz}^a \cdot \nabla_h \zeta.$$

A comparison of the magnitudes of the S_{DEF} and S_{ADV} forcing terms reveals the dominance of S_{ADV} ($S_{DEF}/S_{ADV} \sim 0.4$):

$$f \mathbf{u}_{hz}^a \cdot \nabla_h \zeta > 2f \mathbf{u}_z^g \cdot \nabla_h \zeta + 2\nabla_h \mathbf{u}_h \cdot \nabla_h (\nabla_h b).$$

Hence, the sources of vertical motion are mainly driven by the horizontal advection of vertical relative vorticity by the ageostrophic vertical shear. The importance of including this term in the omega equation was already demonstrated by Viúdez and Dritschel (2004). Pallàs-Sanz and Viúdez (2005) found that the most important forcing term in the generalized omega equation was the horizontal advection of vertical relative vorticity by the total vertical shear. We demonstrate that, for the PUMP eddy, the advection is mainly due to ageostrophic vertical shear.

The horizontal ASC within the PUMP eddy is anticyclonic ($|\mathbf{u}_h| = |\mathbf{u}_h^a + \mathbf{u}^g| > |\mathbf{u}^g|$) and mainly driven by horizontal advective acceleration, which, in turn, is dominated by the centripetal acceleration of the flow. The former methodology used to estimate the horizontal ageostrophic velocity from the residual of the total (ADCP) horizontal velocity and the geostrophic velocity carries some uncertainty associated with the computation of the geostrophic velocity using thermal wind balance. For the PUMP dataset, the anticlockwise rotation of the horizontal advective acceleration within the PUMP eddy core agrees well with the diagnosed horizontal ASC. Hence, the results suggest that this method of obtaining the horizontal ASC from centripetal acceleration is viable but does depend on the quality of the ADCP measurements.

g. Total vertical fluxes

The vertical heat flux is defined as $T'w'$, where $T' = T - \langle T \rangle_H$, $w' = w - \langle w \rangle_H$, and $\langle \rangle_H$ represents the horizontal average within the eddy core. In the same way, the vertical potential vorticity (Π) flux is expressed

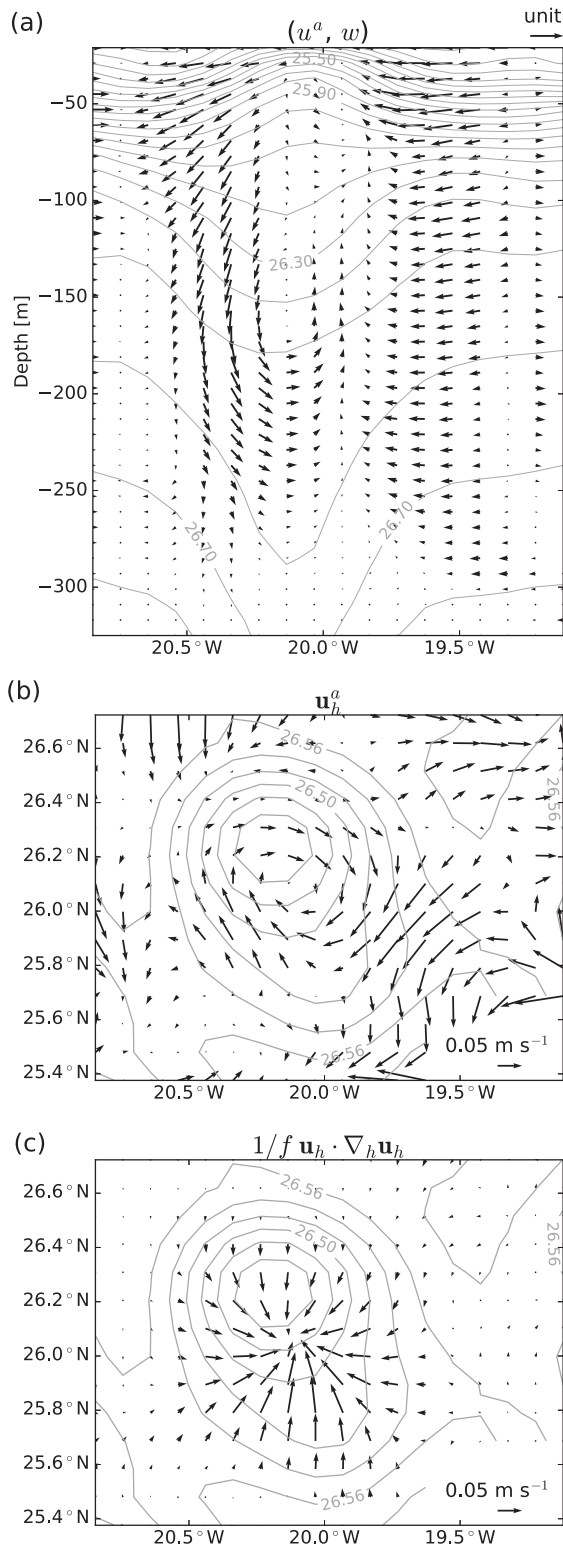


FIG. 10. (a) Vertical section along 26.1°N of the ageostrophic zonal velocity u^a and w . A unit arrow on the map corresponds to 0.1 m s⁻¹ for the zonal component u^a and to 1×10^{-4} m s⁻¹ for the vertical component w . Horizontal distribution at 165-m depth of (b) the horizontal ASC and (c) $(1/f)\mathbf{u}_h \cdot \nabla_h \mathbf{u}_h$. Gray contours represent the potential density anomaly σ_θ , with a contour interval of 0.1 kg m⁻³ in (a).

as $\Pi'w'$. Vertical profiles of the horizontal averages of both fluxes are shown in Fig. 11. The $\langle T'w' \rangle_H$ has negative values between the surface and 100-m depth, indicating that vertical motions act to cool the upper layers. On the other hand, below 200-m depth the horizontally averaged vertical heat flux has positive values, indicating that the vertical velocity is warming the deeper layers. The vertical profile of the horizontal average of the Π flux has negative values in the upper 100 m and is nearly zero below. This indicates a loss of Π in the upper layers. The intrathermocline eddy temperature anomaly field is characterized by a cold cap within the seasonal pycnocline and a deeper warm core between 200- and 500-m depth, while the Π anomaly field is characterized by negative values in the seasonal pycnocline (B. Barceló-Llull et al. 2017). These results suggest that vertical velocity contributes to the maintenance of the typical characteristics of the intrathermocline eddy.

4. Discussion

The vertical velocity distribution within the intrathermocline eddy is mainly characterized by extreme values at the eddy periphery, while at the eddy center vertical motions are negligible (Figs. 3, 4). The DCM distribution reveals higher concentration of chlorophyll-a at the eddy periphery, while at the eddy center the concentration is minimum with values similar to those outside the eddy region (Fig. 5). Annular ring-shaped patterns of CHL have been observed around anticyclones in different regions of the global ocean from satellite data (McGillicuddy 2016; Mizobata et al. (2002) in the Bering Sea, Kahru et al. (2007) in the Southern Ocean, and José et al. (2014) in the Mozambique Channel. To explain this eddy boundary enhancement, two mechanisms have been proposed: lateral entrainment and local enhancement (McGillicuddy 2016). Our results suggest that the higher chlorophyll-a concentration around the PUMP eddy may be due to the deeper upwelling cell (Figs. 3c, 4), which would introduce nutrients to the euphotic layer, while in the upper layers the small upwelling cells would redistribute the nutrients within the euphotic layer. The time expected for biological removal of the introduced nutrients is quicker than that of the vertical velocity supply/subduction (McGillicuddy et al. 1998; Mahadevan et al. 2008). Hence, the upwelled nutrients would be rapidly assimilated by phytoplankton around the eddy periphery and distributed by the horizontal flow that is several orders of magnitude larger than the vertical motions.

Several dynamical mechanisms have been proposed to explain the physical processes responsible for creating the observed biological patterns within mesoscale eddies. According to the eddy pumping mechanism, the

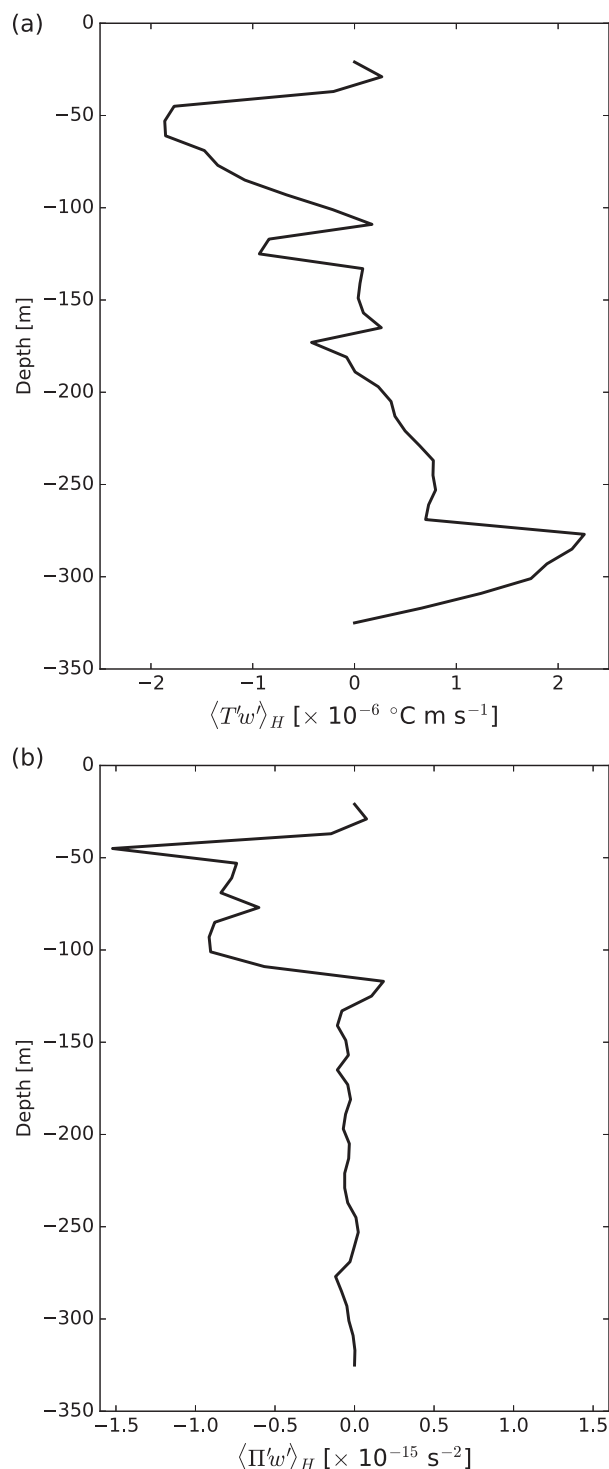


FIG. 11. Horizontally averaged (a) vertical heat flux $\langle T'w' \rangle_H$ and (b) vertical potential vorticity flux $\langle \Pi'w' \rangle_H$ as a function of depth.

doming of the seasonal pycnocline would induce an input of nutrients and high chlorophyll-*a* concentrations within the cores of intrathermocline eddies. This

enhancement has been observed in the Sargasso Sea (McGillicuddy et al. 1998), but it is not the case for the PUMP eddy (Fig. 5). On the other hand, linear Ekman pumping, which predicts a monopole of positive vertical velocities within anticyclonic eddies (Martin and Richards 2001), has been computed for the PUMP eddy and is weaker than the nonlinear contribution to the eddy–wind interaction (Figs. 9c,d). The nonlinear Ekman pumping within the PUMP eddy induces a dipolar distribution of w with maximum values of $\pm 0.5 \text{ m day}^{-1}$ at the base of the Ekman layer, located at 32 m. Hence, the nonlinear Ekman pumping has to be compared with the horizontal distribution of the diagnosed w in the upper layers (Fig. 3a). Its multipolar structure differs from the nonlinear Ekman pumping dipolar pattern; nevertheless, the w_{ADV} contribution within the seasonal pycnocline (Fig. 7b) is also characterized by a dipolar pattern with similar maximum values. Hence, the w distribution in the upper layers may be partly explained by nonlinear Ekman pumping. On the other hand, the w_{DEF} contribution in the upper layers (Fig. 7a) is characterized by an octopolar pattern with alternating upwelling/downwelling cells. Buongiorno Nardelli (2013) proposed vortex Rossby waves as a possible mechanism for modulating the vertical velocity field within mesoscale eddies. Although this hypothesis is difficult to demonstrate, w_{DEF} shows an azimuthal wavelike distribution with a wavenumber of 4.

The w_{ADV} contribution within the depressed main pycnocline has a dipolar structure (Fig. 8b) with a broader and more intense downwelling cell in the west and a weaker upwelling cell in the east. The nonnegligible ageostrophic horizontal velocity over the whole water column (Fig. 10) suggests the possibility of deep wind influence. On the other hand, w_{DEF} has a quadripolar structure (Fig. 8a) already predicted by Viúdez and Dritschel (2003) with a primitive equation model. The w dipolar structure within an intrathermocline eddy was first seen south of Fuerteventura by Benítez-Barrios et al. (2011) from low-resolution in situ data.

5. Conclusions

For the first time we have estimated the ASC within an anticyclonic intrathermocline eddy from high-resolution quasi-synoptical 3D observational data. The intrathermocline eddy is characterized by two different horizontal distributions of w . In the seasonal pycnocline, the w distribution is characterized by alternating upwelling and downwelling cells located at the eddy periphery. Below 85-m depth (main pycnocline), the w distribution changes gradually in depth toward a dipolar pattern with a downwelling cell on the western edge of the eddy and an upwelling cell on the eastern edge of the

eddy. Maximum values of w of -6.4 and 3.4 m day^{-1} are located between 160- and 185-m depth. A similar w magnitude was found by Benítez-Barrios et al. (2011) within an intrathermocline eddy south of Fuerteventura Island. In the upper layers, the w multipolar distribution may be the result of a combination of nonlinear Ekman pumping with modulation by vortex Rossby waves, although the latter is difficult to demonstrate with the available data (Buongiorno Nardelli 2013). The deeper w dipolar distribution suggests the possibility of a deep wind influence through relatively intense ageostrophic vertical shear. The w_{DEF} contribution in the deeper layers has a quadripolar distribution already predicted by theoretical models (Viúdez and Dritschel 2003). The interaction of both contributions w_{DEF} and w_{ADV} gives rise to the final w dipolar distribution already detected from low-resolution data by Benítez-Barrios et al. (2011) in the region of study. The w_{DEF} contribution in the whole water column is mainly dominated by its geostrophic counterpart; hence, the w distribution within the PUMP eddy is mainly driven by both w_{DEFG} and w_{ADV} . These contributions can be interpreted respectively as the horizontal deformation of the density field by the geostrophic velocity and the advection of vertical relative vorticity by the ageostrophic vertical shear.

Our observations from in situ data reveal that a typical intrathermocline eddy under typical atmospheric forcing enhances chlorophyll-*a* concentration, and this enhancement occurs at the eddy periphery instead of at the eddy center. This coincides with the occurrence of upwelling cells along the eddy periphery that may bring nutrients to the euphotic layer. Our analysis suggests that part of these cells may be result of eddy-wind interaction through nonlinear Ekman pumping, but also other processes may be at work, such as the plausible occurrence of vortex Rossby waves.

The horizontal ageostrophic velocity acts to close the dipolar vertical velocity distribution within the intrathermocline eddy. The anticyclonic horizontal ASC is proportional to the anticlockwise rotation of the horizontal advective acceleration, which is mainly dominated by the centripetal acceleration. Vertical velocities maintain the intrathermocline eddy structure through fluxes of heat and potential vorticity. The vertical velocity acts to cool the upper layers and warm the deeper layers, while contributing to a loss of potential vorticity in the seasonal pycnocline.

Though more experimental studies are needed to corroborate the generality of these results, we conclude that the dipolar distribution of mesoscale vertical velocity in the PUMP eddy is robust and may be ubiquitous in wind-forced and elliptically shaped anticyclonic intrathermocline eddies in the Canary Eddy Corridor.

This result contrasts with the quadripolar distribution of w expected in an f plane and nonforced numerical elliptical anticyclone (Viúdez and Dritschel 2003). The reasons for this difference between theory and observations are expected to be a source of future work.

Acknowledgments. This work has been carried out as part of the PUMP (CTM2012-33355) project funded by the Spanish National Research Program. Bàrbara Barceló-Llull is supported by a doctoral grant from the Spanish National Research Program associated with the PUMP project (BES-2013-065459). This work has been also supported by the FLUXES (CTM2015-69392-C3-3-R) project funded by the Spanish National Research Program and the European Regional Development Fund (MINECO-FEDER). We express our gratitude to the technical staff (UTM-CSIC) and crew of R/V *BIO Hespérides* for supporting our work at sea.

REFERENCES

- Allen, J. T., and D. A. Smeed, 1996: Potential vorticity and vertical velocity at the Iceland-Farøes Front. *J. Phys. Oceanogr.*, **26**, 2611–2634, doi:10.1175/1520-0485(1996)026<2611:PVAVVA>2.0.CO;2.
- , —, A. J. G. Nurser, J. W. Zhang, and M. Rixen, 2001: Diagnosis of vertical velocities with the QG omega equation: An examination of the errors due to sampling strategy. *Deep-Sea Res.*, **48**, 315–346, doi:10.1016/S0967-0637(00)00035-2.
- Badin, G., 2012: Surface semi-geostrophic dynamics in the ocean. *Geophys. Astrophys. Fluid Dyn.*, **107**, 526–540, doi:10.1080/03091929.2012.740479.
- Barceló-Llull, B., E. Mason, A. Capet, and A. Pascual, 2016: Impact of vertical and horizontal advection on nutrient distribution in the southeast Pacific. *Ocean Sci.*, **12**, 1003–1011, doi:10.5194/os-12-1003-2016.
- , and Coauthors, 2017: Anatomy of a subtropical intrathermocline eddy. *Deep-Sea Res. I*, doi:10.1016/j.dsr.2017.03.012, in press.
- Benítez-Barrios, V., J. L. Pelegrí, A. Hernández-Guerra, K. M. M. Lwiza, D. Gomis, P. Vélez-Belchí, and S. Hernández-León, 2011: Three-dimensional circulation in the NW Africa coastal transition zone. *Prog. Oceanogr.*, **91**, 516–533, doi:10.1016/j.pocean.2011.07.022.
- Bretherton, F. P., R. E. Davis, and C. B. Fandry, 1976: A technique for objective analysis and design of oceanographic experiments applied to MODE-73. *Deep-Sea Res. Oceanogr. Abstr.*, **23**, 559–582, doi:10.1016/0011-7471(76)90001-2.
- Buongiorno Nardelli, B., 2013: Vortex waves and vertical motion in a mesoscale cyclonic eddy. *J. Geophys. Res. Oceans*, **118**, 5609–5624, doi:10.1002/jgrc.20345.
- , R. Santoleri, and S. Sparnocchia, 2001: Small mesoscale features at a meandering upper-ocean front in the western Ionian Sea (Mediterranean Sea): Vertical motion and potential vorticity analysis. *J. Phys. Oceanogr.*, **31**, 2227–2250, doi:10.1175/1520-0485(2001)031<2227:SMFAAM>2.0.CO;2.
- Calil, P. H. R., and K. J. Richards, 2010: Transient upwelling hot spots in the oligotrophic North Pacific. *J. Geophys. Res.*, **115**, C02003, doi:10.1029/2009JC005360.

- Chelton, D. B., and S.-P. Xie, 2010: Coupled ocean-atmosphere interaction at oceanic mesoscales. *Oceanography*, **23**, 52–69, doi:10.5670/oceanog.2010.05.
- D'Asaro, E., C. Lee, L. Rainville, R. Harcourt, and L. Thomas, 2011: Enhanced turbulence and energy dissipation at ocean fronts. *Science*, **332**, 318–322, doi:10.1126/science.1201515.
- Durran, D. R., and L. W. Snellman, 1987: The diagnosis of synoptic-scale vertical motion in an operational environment. *Wea. Forecasting*, **2**, 17–31, doi:10.1175/1520-0434(1987)002<0017:TDOSSV>2.0.CO;2.
- Feistel, R., 2003: A new extended Gibbs thermodynamic potential of seawater. *Prog. Oceanogr.*, **58**, 43–114, doi:10.1016/S0079-6611(03)00088-0.
- , 2008: A Gibbs function for seawater thermodynamics for -6 to 80°C and salinity up to 120 g kg^{-1} . *Deep-Sea Res. I*, **55**, 1639–1671, doi:10.1016/j.dsr.2008.07.004.
- Firing, E., J. Ranada, and P. Caldwell, 1995: Processing ADCP data with the CODAS software system version 3.1. Joint Institute for Marine and Atmospheric Research, University of Hawaii & National Oceanographic Data Center Rep., 218 pp.
- Gaube, P., D. B. Chelton, P. G. Strutton, and M. J. Behrenfeld, 2013: Satellite observations of chlorophyll, phytoplankton biomass, and Ekman pumping in nonlinear mesoscale eddies. *J. Geophys. Res. Oceans*, **118**, 6349–6370, doi:10.1002/2013JC009027.
- , D. J. McGillicuddy Jr., D. B. Chelton, M. J. Behrenfeld, and P. G. Strutton, 2014: Regional variations in the influence of mesoscale eddies on near-surface chlorophyll. *J. Geophys. Res. Oceans*, **119**, 8195–8220, doi:10.1002/2014JC010111.
- , D. B. Chelton, R. M. Samelson, M. G. Schlax, and L. W. O'Neill, 2015: Satellite observations of mesoscale eddy-induced Ekman pumping. *J. Phys. Oceanogr.*, **45**, 104–132, doi:10.1175/JPO-D-14-0032.1.
- Giordani, H., L. Prieur, and G. Caniaux, 2006: Advanced insights into sources of vertical velocity in the ocean. *Ocean Dyn.*, **56**, 513–524, doi:10.1007/s10236-005-0050-1.
- Hansen, D. V., and C. A. Paul, 1987: Vertical motion in the eastern equatorial Pacific inferred from drifting buoys. *Oceanol. Acta*, **1987**, 27–32. [Available online at <http://archimer.ifremer.fr/doc/00267/37843/35924.pdf>]
- Harcourt, R. R., E. L. Steffen, R. W. Garwood, and E. A. D'Asaro, 2002: Fully Lagrangian floats in Labrador Sea deep convection: Comparison of numerical and experimental results. *J. Phys. Oceanogr.*, **32**, 493–510, doi:10.1175/1520-0485(2002)032<0493:FLFILS>2.0.CO;2.
- Holm-Hansen, O., C. J. Lorenzen, R. W. Holmes, and J. D. H. Strickland, 1965: Fluorometric determination of chlorophyll. *ICES J. Mar. Sci.*, **30**, 3–15, doi:10.1093/icesjms/30.1.3.
- Hoskins, B. J., and F. P. Bretherton, 1972: Atmospheric frontogenesis models: Mathematical formulation and solution. *J. Atmos. Sci.*, **29**, 11–37, doi:10.1175/1520-0469(1972)029<0011:AFMMFA>2.0.CO;2.
- , and I. Draghici, 1977: The forcing of ageostrophic motion according to the semi-geostrophic equations and in an isentropic coordinate model. *J. Atmos. Sci.*, **34**, 1859–1897, doi:10.1175/1520-0469(1977)034<1859:TFOAMA>2.0.CO;2.
- , —, and H. C. Davies, 1978: A new look at the ω -equation. *Quart. J. Roy. Meteor. Soc.*, **104**, 31–38, doi:10.1002/qj.49710443903.
- José, Y. S., O. Aumont, E. Machu, P. Penven, C. L. Moloney, and O. Maury, 2014: Influence of mesoscale eddies on biological production in the Mozambique Channel: Several contrasted examples from a coupled ocean-biogeochemistry model. *Deep-Sea Res.*, **100**, 79–93, doi:10.1016/j.dsr2.2013.10.018.
- Kahru, M., B. G. Mitchell, S. T. Gille, C. D. Hewes, and O. Holm-Hansen, 2007: Eddies enhance biological production in the Weddell-Scotia Confluence of the Southern Ocean. *Geophys. Res. Lett.*, **34**, L14603, doi:10.1029/2007GL030430.
- Klein, P., and G. Lapeyre, 2009: The oceanic vertical pump induced by mesoscale and submesoscale turbulence. *Annu. Rev. Mar. Sci.*, **1**, 351–375, doi:10.1146/annurev.marine.010908.163704.
- Large, W. G., 1979: The turbulent fluxes of momentum and sensible heat over the open sea during moderate to strong winds. Ph.D. thesis, University of British Columbia, 193 pp.
- Le Traon, P.-Y., 1990: A method for optimal analysis of fields with spatially-variable mean. *J. Geophys. Res.*, **95**, 13 543–13 547, doi:10.1029/JC095iC08p13543.
- Lindstrom, S. S., and D. P. Watts, 1994: Vertical motion in the Gulf Stream near 68°W . *J. Phys. Oceanogr.*, **24**, 2321–2333, doi:10.1175/1520-0485(1994)024<2321:VMITGS>2.0.CO;2.
- Mahadevan, A., and A. Tandon, 2006: An analysis of mechanisms for submesoscale vertical motion at ocean fronts. *Ocean Modell.*, **14**, 241–256, doi:10.1016/j.ocemod.2006.05.006.
- , L. N. Thomas, and A. Tandon, 2008: Comment on “Eddy/wind interactions stimulate extraordinary mid-ocean plankton blooms.” *Science*, **320**, 448, doi:10.1126/science.1152111.
- Martin, A. P., and K. J. Richards, 2001: Mechanisms for vertical nutrient transport within a North Atlantic mesoscale eddy. *Deep-Sea Res. II*, **48**, 757–773, doi:10.1016/S0967-0645(00)00096-5.
- McGillicuddy, D. J., 2016: Mechanisms of physical-biological-biogeochemical interaction at the oceanic mesoscale. *Annu. Rev. Mar. Sci.*, **8**, 125–159, doi:10.1146/annurev-marine-010814-015606.
- , and Coauthors, 1998: Influence of mesoscale eddies on new production in the Sargasso Sea. *Nature*, **394**, 263–266, doi:10.1038/28367.
- , and Coauthors, 2007: Eddy wind interactions stimulate extraordinary mid-ocean plankton blooms. *Science*, **316**, 1021–1026, doi:10.1126/science.1136256.
- , J. R. Ledwell, and L. A. Anderson, 2008: Response to comment on “Eddy/wind interactions stimulate extraordinary mid-ocean plankton blooms.” *Science*, **320**, 448, doi:10.1126/science.1148974.
- McWilliams, J. C., L. P. Graves, and M. T. Montgomery, 2003: A formal theory for vortex Rossby waves and vortex evolution. *Geophys. Astrophys. Fluid Dyn.*, **97**, 275–309, doi:10.1080/0309192031000108698.
- Mizobata, K., and Coauthors, 2002: Bering Sea cyclonic and anticyclonic eddies observed during summer 2000 and 2001. *Prog. Oceanogr.*, **55**, 65–75, doi:10.1016/S0079-6611(02)00070-8.
- Nagai, T., A. Tandon, and D. L. Rudnick, 2006: Two-dimensional ageostrophic secondary circulation at ocean fronts due to vertical mixing and large-scale deformation. *J. Geophys. Res.*, **111**, C09038, doi:10.1029/2005JC002964.
- Naveira Garabato, A. C., H. Leach, J. T. Allen, R. T. Pollard, and V. H. Strass, 2001: Mesoscale subduction at the Antarctic polar front driven by baroclinic instability. *J. Phys. Oceanogr.*, **31**, 2087–2107, doi:10.1175/1520-0485(2001)031<2087:MSATAP>2.0.CO;2.
- Pallàs-Sanz, E., and A. Viúdez, 2005: Diagnosing mesoscale vertical motion from horizontal velocity and density data. *J. Phys. Oceanogr.*, **35**, 1744–1762, doi:10.1175/JPO2784.1.
- , and —, 2007: Three-dimensional ageostrophic motion in mesoscale vortex dipoles. *J. Phys. Oceanogr.*, **37**, 84–105, doi:10.1175/JPO2978.1.
- , T. M. S. Johnston, and D. L. Rudnick, 2010a: Frontal dynamics in a California Current System shallow front: 1. Frontal

- processes and tracer structure. *J. Geophys. Res.*, **115**, C12067, doi:10.1029/2009JC006032.
- , —, and —, 2010b: Frontal dynamics in a California Current System shallow front: 2. Mesoscale vertical velocity. *J. Geophys. Res.*, **115**, C12068, doi:10.1029/2010JC006474.
- Pascual, A., S. Ruiz, B. Buongiorno Nardelli, S. Guinehut, D. Iudicone, and J. Tintoré, 2015: Net primary production in the Gulf Stream sustained by quasi-geostrophic vertical exchanges. *Geophys. Res. Lett.*, **42**, 441–449, doi:10.1002/2014GL062569.
- Pedder, M. A., and A. J. Thorpe, 1999: The semi-geostrophic diagnosis of vertical motion. I: Formulation and coordinate transformations. *Quart. J. Roy. Meteor. Soc.*, **125**, 1231–1256, doi:10.1002/qj.1999.49712555607.
- Pinot, J.-M., J. Tintoré, and D.-P. Wang, 1996: A study of the omega equation for diagnosing vertical motions at ocean fronts. *J. Mar. Res.*, **54**, 239–259, doi:10.1357/0022240963213358.
- Pollard, R. T., and L. A. Regier, 1992: Vorticity and vertical circulation at an ocean front. *J. Phys. Oceanogr.*, **22**, 609–625, doi:10.1175/1520-0485(1992)022<0609:VAVCAA>2.0.CO;2.
- Rodríguez, J., and Coauthors, 2001: Mesoscale vertical motion and the size structure of phytoplankton in the ocean. *Nature*, **410**, 360–363, doi:10.1038/35066560.
- Rudnick, D. L., 1996: Intensive surveys of the Azores front: 2. Inferring the geostrophic and vertical velocity fields. *J. Geophys. Res.*, **101**, 16 291–16 303, doi:10.1029/96JC01144.
- Sangrà, P., and Coauthors, 2009: The Canary Eddy Corridor: A major pathway for long-lived eddies in the subtropical North Atlantic. *Deep-Sea Res.*, **56**, 2100–2114, doi:10.1016/j.dsr.2009.08.008.
- Schultz Tokos, K. L., H.-H. Hinrichsen, and W. Zenk, 1994: Merging and migration of two meddies. *J. Phys. Oceanogr.*, **24**, 2129–2141, doi:10.1175/1520-0485(1994)024<2129:MAMOTM>2.0.CO;2.
- Shcherbina, A. Y., and Coauthors, 2015: The LatMix summer campaign: Submesoscale stirring in the upper ocean. *Bull. Amer. Meteor. Soc.*, **96**, 1257–1279, doi:10.1175/BAMS-D-14-00015.1.
- Shearman, R. K., J. A. Barth, J. S. Allen, and R. L. Haney, 2000: Diagnosis of the three-dimensional circulation in mesoscale features with large Rossby number. *J. Phys. Oceanogr.*, **30**, 2687–2709, doi:10.1175/1520-0485(2001)031<2687:DOTTDC>2.0.CO;2.
- Skamarock, W. C., and Coauthors, 2008: A description of the Advanced Research WRF version 3. NCAR Tech. Note NCAR/TN-475+STR, 113 pp., doi:10.5065/D68S4MVH.
- Spall, M. A., 1997: Baroclinic jets in confluent flow. *J. Phys. Oceanogr.*, **27**, 1054–1071, doi:10.1175/1520-0485(1997)027<1054:BJICF>2.0.CO;2.
- Stern, M. E., 1965: Interaction of a uniform wind stress with a geostrophic vortex. *Deep-Sea Res. Oceanogr. Abstr.*, **12**, 355–367, doi:10.1016/0011-7471(65)90007-0.
- Thomas, L. N., C. M. Lee, and Y. Yoshikawa, 2010: The subpolar front of the Japan/East Sea. Part II: Inverse method for determining the frontal vertical circulation. *J. Phys. Oceanogr.*, **40**, 3–25, doi:10.1175/2009JPO4018.1.
- Tintoré, J., D. Gomis, S. Alonso, and G. Parrilla, 1991: Mesoscale dynamics and vertical motion in the Alborán Sea. *J. Phys. Oceanogr.*, **21**, 811–823, doi:10.1175/1520-0485(1991)021<0811:MDAVMI>2.0.CO;2.
- Trenberth, K. E., 1978: On the interpretation of the diagnostic quasi-geostrophic omega equation. *Mon. Wea. Rev.*, **106**, 131–137, doi:10.1175/1520-0493(1978)106<0131:OTIOTD>2.0.CO;2.
- Viúdez, A., and D. G. Dritschel, 2003: Vertical velocity in mesoscale geophysical flows. *J. Fluid Mech.*, **483**, 199–223, doi:10.1017/S0022112003004191.
- , and —, 2004: Potential vorticity and the quasigeostrophic and semigeostrophic mesoscale vertical velocity. *J. Phys. Oceanogr.*, **34**, 865–887, doi:10.1175/1520-0485(2004)034<0865:PVATQA>2.0.CO;2.
- , J. Tintoré, and R. L. Haney, 1996: About the nature of the generalized omega equation. *J. Atmos. Sci.*, **53**, 787–795, doi:10.1175/1520-0469(1996)053<0787:ATNOTG>2.0.CO;2.